

A Competitive n-Type OECT Material via Copolymerization of Electron Deficient Building Blocks

Andreas Erhardt, Adrian Hochgesang, Christopher R. McNeill, and Mukundan Thelakkat*

The classical acceptor motifs diketopyrrolopyrrole (DPP) and thienopyrrolodione (TPD) are copolymerized to yield the acceptor–acceptor polymer “Poly(DPP-TPD).” The fundamental design idea is to maximize the electron affinity (EA), thus increasing the ambient stability of the reduced state against oxygen and water while ensuring high ion compatibility through the incorporation of hydrophilic oligoethylene glycol N-substituents. Additionally, a highly planarized polymer structure is anticipated, due to the extended noncovalent interactions (conformational locking) between the carbonyl oxygen and the thiophene protons. Cyclic voltammetry, spectroelectrochemistry, ultraviolet photoelectron spectroscopy, ultraviolet-visible absorption spectroscopy, and organic field effect transistor (OFET) characterization demonstrate the suitability for n-type organic electrochemical transistor (OECT) devices. High EA, ionization potential, and good electron mobility ($\mu_{e(\text{OFET})}$) are shown, in addition to the electrochemical reduction of polymer films in aqueous electrolyte. In n-type OECTs, poly(DPP-TPD) demonstrates a moderate threshold voltage of $V_{\text{th}} = 0.58 \text{ V}$ and an outstanding μC^* value of $7.62 \text{ F cm}^{-1} \text{ V}^{-1} \text{ s}^{-1}$. Cycling studies consisting of pulsed on- and off-switching of the device at gate voltages between $V_g = 0.6\text{--}0.8 \text{ V}$ in the saturation regime reveal high stability for more than 2700 cycles with rapid switching kinetics.

1. Introduction

Organic semiconductors are an emerging class of materials, based on materials with conjugated motifs, resulting in semiconducting properties, macroscopically reminiscent of classical inorganic semiconductors.^[1] One of the key advantages of organic semiconductors is their flexibility, which allows for the development of light-weight devices that can conform to various shapes and sizes.^[2,3] This as well as the mechanical similarity of organic semiconductors to biological tissue makes organic semiconductors appealing candidates at the juncture between biological and electronic in vivo applications.^[4,5]

One class of bioelectronic devices, which can only be operated with organic semiconductors as active layer materials, are organic electrochemical transistors (OECTs). An OECT consists of a semiconducting polymer layer, connecting a source- and drain electrode, and switched via an electrolyte-immersed gate electrode.^[6] For this type of thin film transistor, organic mixed ionic-electronic conductor (OMIEC) materials are employed as active layers.


This means that along with electronic conduction, the accommodation of ionic charges is required.^[7] Under the application of a source-gate bias, the OMIEC is oxidized (in p-type materials), or reduced (in n-type materials), resulting in charged and conductive polymers. Charge compensation is possible through electrolyte ions, diffusing into the material, resulting in volumetric capacity and electronic conductivity in the swollen state. Due to the charge accumulation under applied gate potential, this way of operation is commonly referred to as *accumulation mode*.^[8] A priori-doped materials, such as poly(3,4-ethylenedioxythiophene) polystyrene sulfonate (PEDOT:PSS), can also be dedoped this way, resulting in inverted device operation (“*depletion mode*”).^[9,10] The quantification of material performance is commonly conducted according to the benchmarking approach of Rivnay and Inal and is focused on the optimization of the device-architecture independent transconductance (dI/dV), which is directly proportional to the product of the charge carrier mobility μ in the swollen state and the volumetric capacitance C^* , as described by Equation (1).^[11]

$$dI/dV = g_m = Wd / L\mu C^*(V_{\text{th}} - V_g) \quad (1)$$

A. Erhardt, A. Hochgesang, M. Thelakkat
 Applied Functional Polymers
 University of Bayreuth
 Universitätsstraße 30, 95447 Bayreuth, Germany
 E-mail: mukundan.thelakkat@uni-bayreuth.de

A. Erhardt, C. R. McNeill
 Department of Materials Engineering
 Monash University
 20 Research Way, Clayton, Victoria 3800, Australia

M. Thelakkat
 Bavarian Polymer Institute
 University of Bayreuth
 Universitätsstraße 30, 95447 Bayreuth, Germany

 The ORCID identification number(s) for the author(s) of this article can be found under <https://doi.org/10.1002/aelm.202300026>.

© 2023 The Authors. Advanced Electronic Materials published by Wiley-VCH GmbH. This is an open access article under the terms of the Creative Commons Attribution License, which permits use, distribution and reproduction in any medium, provided the original work is properly cited.

DOI: 10.1002/aelm.202300026

Recent reports point out the importance of further material parameters, such as threshold voltage (V_{th}) response time, subthreshold swing, and cycling stability.^[9,12,13] In the palette of OMIEC materials, an abundance of highly stable accumulation mode p-type materials with decent performance, as per μC^* quantification, is known.^[14] The best-performing n-type materials, in contrast, are all derived either from naphthalene diimide (NDI) derivatives or polymers with extended fused-ring systems and exhibit relatively low stability and transconductance.^[15,16] Based on these materials, fundamental questions, such as the impact of side chain length, comonomer compositions, and side chain hydrophilicity, were elucidated and understood.^[17] However, high-performing n-type polymers for OECT based on further backbone motifs are sparse. Fused-ring systems are in a much earlier stage of development and may therefore help advance the field further. Due to the stiff nature of the fused-ring polymer backbone, the low solubility of those materials is an intrinsic disadvantage of this material class. We thus aimed for a new n-type OMIEC which is neither based on an NDI-based nor fused ring motif. As described previously, the stability issues of n-type polymers originate from insufficiently high electron affinities (or insufficiently low lowest unoccupied molecular orbital (LUMO) levels) of the materials.^[18,19] The low μC^* of most n-type polymers further was concluded to be caused by low charge carrier mobility.^[11] Based on these factors, we designed an acceptor–acceptor copolymer to lower the LUMO, while aiming for a planarized molecular structure. To mimic the bulk properties of ladder-type polymers, we chose two acceptor monomers diketopyrrolopyrrole (DPP) and thienopyrrolodione (TPD), that are known to form planarized structures in the solid state, caused by noncovalent interactions between the thiophene protons and carbonyl oxygen atoms.^[6–9,20–23] By alternation of hydrogen bond donor and acceptor, a quasi-ladder type polymer in the solid state is anticipated. To ensure ion compatibility as well as sufficient solubility both monomers are equipped with triethylene glycol substituents.^[17,24]

2. Results and Discussion

The monomers DPP and TPD were chosen based on their role as acceptor components in traditional donor–acceptor (D-A) copolymers, which were in turn reported to exhibit high planarity and charge carrier mobility.^[23,25–28] As previously stated, both monomers were reported to exhibit strong noncovalent interactions, leading to backbone planarization of the respective polymers in the solid state. Such conformational locks were reported to lead to electronic properties, similar to ladder type-polymers.^[29] As these interactions are noncovalent and dynamic in nature, the drawback of ladder-type polymers of drastically reduced solubility can be avoided or at least weakened. For DPP, the aromatic unit, attached directly to the dilactam unit, can promote, or disrupt planarization, and additionally influence the optoelectronic properties decisively.^[23,27] We equipped the DPP monomer with thiophene flanking units, which are known to exhibit low dihedral angles to the lactam unit.^[22] The molecular geometry of such poly(DPP-TPD) copolymers was previously simulated by the group of LeClerc and was shown

to exhibit relatively low dihedral angles.^[30] This hydrophilic A-A type copolymer based on a DPP-thiophene-TPD backbone is synthesized via a streamlined direct arylation procedure and subsequently characterized with respect to its basic thermal and optoelectronic properties, film morphology, as well as OECT device performance and stability.

2.1. Synthesis

The DPP chromophore was synthesized according to Müller et al. with the side chain substitution and bromination procedures from Krauss et al.^[23,31] TPD synthesis was adapted and optimized, starting from the procedure of Reynolds et al.^[32]

For polymerization, direct arylation polymerization (DAP) was employed, following general Ozawa-derived conditions. Previous reports, e.g., by LeClerc were used as starting point for optimization but had to be adapted in respect of reaction solvent, time, temperature, heat source, reactant concentration, and ratio.^[30] High conversions and molecular mass polymers were obtained by reactions in aromatic hydrophobic solvents such as toluene or xylenes, while polymerization attempts in polar solvents such as N-methyl-2-pyrrolidone or dimethylacetamide resulted in the formation of oligomers, despite the higher solubility of the monomers. The use of *o*-xylene with a high reaction molarity of 2.5 mol L⁻¹ enabled microwave-assisted synthesis of the hydrophilic polymer, minimizing polymerization time, and avoiding the use of superheated solvents. Catalyst and oligomer removal was conducted via Soxhlet extraction and precipitation, resulting in the polymer poly(DPP-TPD), as evidenced by the spectroelectrochemistry (SEC) trace in **Figure 1** and the broad ¹H-NMR signals in Figure S1 in the Supporting Information, characteristic of polymers. The exact synthetic procedures are described in the Experimental Section.

2.2. Thermal Properties and Morphology

It is commonly assumed that for OECT application, a balance between crystalline and amorphous domains plays a decisive role, as electronic transport takes place preferentially in the former, ion transport, and storage in the latter. While this is a simplified description of the fundamental processes, it sufficiently demonstrates that crystallinity and morphology play a role in mixed conduction.

To investigate crystallinity as well as melting and crystallization of poly(DPP-TPD), flash differential scanning calorimetry (flash DSC) was employed with heating and cooling rates between 50 and 2000 K s⁻¹ since no transition was observed in conventional DSC. While flash DSC technique is not suitable to determine the real melting point and degree of crystallinity of a material, based on one measurement, its outstanding sensitivity makes it suitable for the detection of weakly pronounced melting transitions. The high scanning speed or short measurement times, enable investigation of thermal transitions above the materials degradation temperature at $T_{5\%} = 305$ °C (cf. thermogravimetric analysis (TGA), Figure S2a, Supporting Information). As shown in Figure S2b in the Supporting Information, however, no melting or crystallization can be detected,

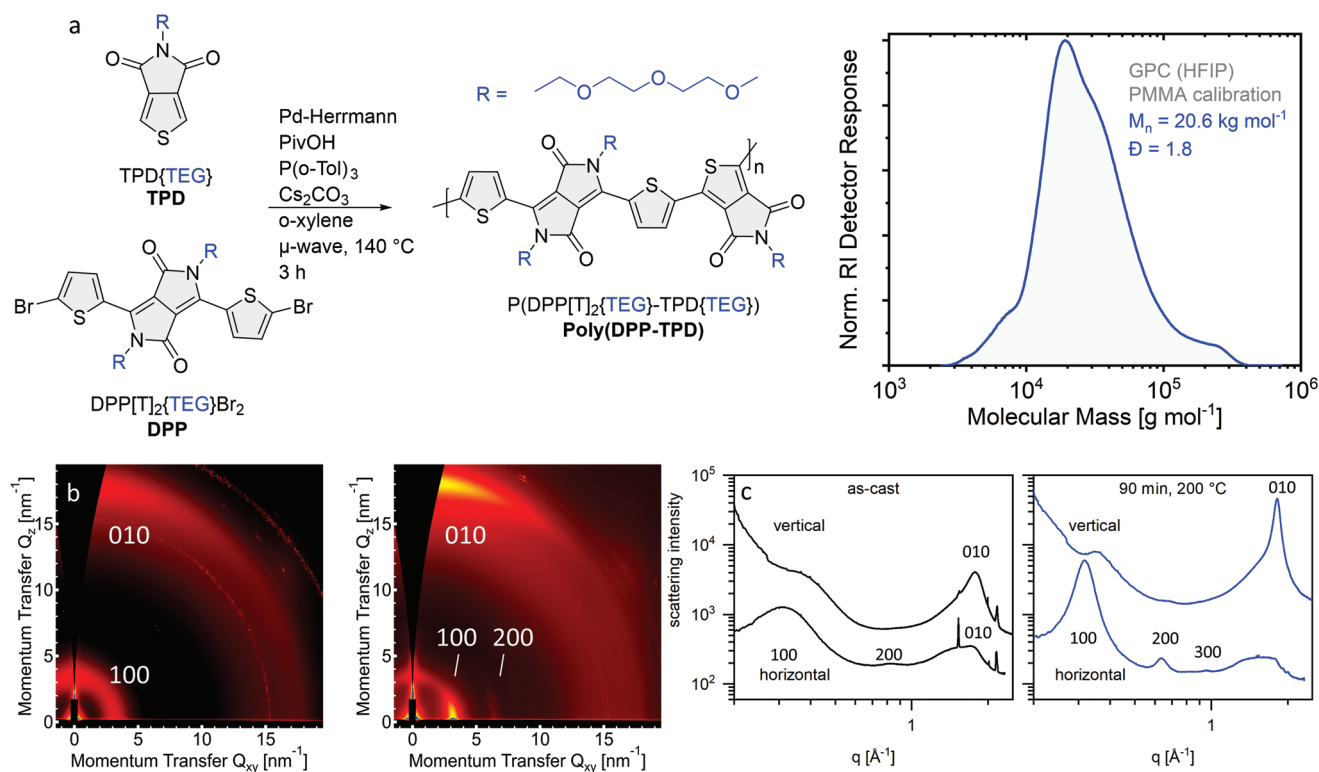


Figure 1. a) Synthesis of the hydrophilic acceptor–acceptor copolymer P(DPP[T]₂{TEG}-TPD{TEG})/poly(DPP-TPD) via direct arylation polymerization and the gel permeation chromatography (GPC) trace of the purified material (hexafluoroisopropanol (HFIP), polymethyl methacrylate (PMMA) calibration). b) GIWAXS images of poly(DPP-TPD), as-cast and annealed for 90 min at 200 °C. c) Vertical and horizontal line profiles (20° width) of the GIWAXS patterns of the polymer poly(DPP-TPD) as-cast and annealed for 90 min at 200 °C.

which could lead to the impression that the material is either amorphous or exhibits a melting transition at temperatures outside the measurement range. As DSC does not detect crystallinity per se, but rather the associated thermal transitions, a more direct method, namely grazing incidence wide-angle X-ray scattering (GIWAXS), was employed to investigate poly(DPP-TPD) films (Figure 1b). As-cast polymer films show weakly pronounced 100 and 010 peaks as well as a relatively intensive anisotropic amorphous halo, which qualitatively demonstrates the weakly ordered nature of the polymer in the pristine state. The horizontal and vertical cake cuts depicted in Figure 1c with an integration width of 20° indicate a weak anisotropy of the 010 peak, which corresponds to a modest preferential face-on chain orientation. Upon annealing for 90 min at 200 °C, both 100 and 010 peaks increase significantly in intensity, revealing additional higher order 200 and 300 peaks as well as a pronounced face-on orientation of the polymer crystallites. This is indicative of an increase in order during the annealing procedure. Further, a decreased peak width of all signals is indicative of an increase in coherence length, which in turn is either caused by an increase in crystallite size and/or a decrease in the degree of paracrystalline disorder. The full width at half maximum (FWHM) of the signals as well as the respective coherence lengths determined via the Scherrer equation are listed in Table S1 in the Supporting Information. Additionally, an underlying halo of isotropic amorphous domains can still be observed. Also listed are the 100 and 010 distances that decrease upon annealing, attrib-

uted to a thermally enabled contraction of the π - π and lamellar distance, which in turn leads to a decreasing unit cell size. Complementary to GIWAXS, the topology of poly(DPP-TPD) film was investigated based on scanning electron microscopy and atomic force microscopy (AFM) imaging and the results are given in Figure S3 in the Supporting Information. Upon high magnification, only holes in the film, caused by the fast-evaporating solvent, are observable. In the AFM phase image of the annealed film, weakly ordered assemblies are visible. However, it is not possible to identify any characteristic lamellar or nanofibril structures usually expected from highly ordered aggregates of conjugated polymers.

2.3. Optoelectronic Properties

For alternating D-A conjugated copolymers, the highest occupied molecular orbital (HOMO) level is predominantly determined by the more electron-rich repeating unit, while the LUMO is mainly decided by the more electron-deficient moiety.^[21,33] This leads to the typical low optical gap of D-A type polymers and the resulting low energy ground state absorption. Here, however, both units are electron deficient (A-type), possibly rendering the push-pull effect less pronounced than in standard D-A copolymers. To determine the optical properties of the copolymer, UV–vis spectroscopy in solution and solid state was recorded.

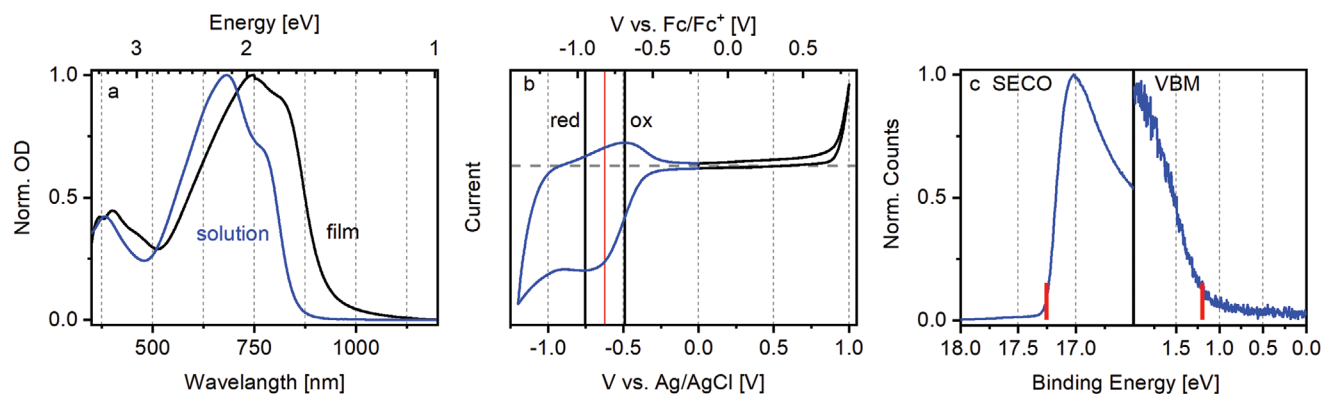


Figure 2. a) UV-vis absorption of a poly(DPP-TPD) thin film and solution in hexafluoro-2-propanol. b) Reduction process of a poly(DPP-TPD) thin film, detected via CV in 0.1 M KCl (aq.). c) SECO and VBM, determined via UPS measurements.

As shown in **Figure 2a**, the polymer absorbs light in the red-near infrared (NIR) region, with a pronounced ground state peak at $\lambda = 670$ nm (solution) and $\lambda = 750$ nm (film), accompanied by a minor absorption at $\lambda = 380$ or 400 nm. This shows that despite the lack of donor units, the acceptor-acceptor copolymers exhibit a sufficiently strong push-pull effect to result in a relatively small optical gap of ≈ 1.33 eV. Further, both in the solid state and solution, pronounced aggregation features can be seen.

As electron transport is facilitated by the occupation of the LUMO with a generated or injected electron, low electron affinity (EA) is predominantly decisive for such a process of electron injection or acceptance and electron transport. For EA determination, cyclic voltammetry (CV) using a three-electrode setup was employed. To gain representative data for the intended application in OECT devices, the polymers were characterized as films in contact with an aqueous 0.1 M KCl electrolyte. As shown in **Figure 2b**, reduction and reoxidation were detectable at -0.75 and -0.49 eV versus Ag/AgCl, respectively. From the halfway potential, as well as the reference couple Fc/Fc⁺, a LUMO level of -4.0 eV was determined. Differential pulse voltammetry (DPV) in acetonitrile containing tetrabutylammonium tetrafluoroborate (TBABF) (0.1 M) indicates an LUMO level of -4.15 eV (cf. **Figure S4a**, Supporting Information). The small discrepancy between the DPV and CV data can be explained due to various degrees of stabilization of the radical anion in the two different solvent media

As evident in **Figure 2b**, no oxidation was detectable during CV studies of poly(DPP-TPD). To still determine the solid-state ionization potential (IP) of the polymer, ultraviolet photoelectron spectroscopy (UPS) was employed. While this method is not fully comparable with swollen OECT operation conditions, it is a more precise method than CV for the determination of IP in general, as it directly measures the energy levels of occupied valence band states with respect to the vacuum level in the solid state. In **Figure 2c**, the secondary electron cutoff (SECO) and valence band maximum (VBM) edge of poly(DPP-TPD) with their onset energies are depicted. The spectrometer work function is calibrated such that it is located at 0 eV (see the Supporting Information), hence the work function of poly(DPP-TPD) is calculated by subtracting the absolute position of the SECO from the He I light source energy (21.22 eV). Accordingly, the work function of poly(DPP-TPD) was determined to

be (3.9 ± 0.1) eV. Adding the VBM position to the work function then yields the IP. From the VBM and SECO edge onset, the IP was determined to be (5.2 ± 0.1) eV. From CV, DPV, and UPS experiments, a bandgap of ≈ 1.2 eV can be derived, similar to the optical bandgap of ≈ 1.33 eV (**Figure 2a**). The low EA and IP confirm the acceptor-acceptor-like character, significantly lowering both frontier orbital energies compared to donor-acceptor copolymers.^[34]

Electrochemical reduction of poly(DPP-TPD) is accompanied by a change of UV-vis absorption which is monitored via spectroelectrochemical (SEC) analysis. For this, films of poly(DPP-TPD) are deposited on conductive indium tin oxide (ITO) substrates and stepwise reduced in a potential range between $V = 0$ and $V = -0.8$ V, followed by reoxidation by increasing the potential to $V = 0$ V again. At an onset of $V = -0.3$ V, the ground state absorption ($\lambda = 740$ nm) decreases, accompanied by the appearance of a polaron absorption ($\lambda = 1050$ nm). In **Figure 3a,b**, the UV-vis spectra of the electrochemical reduction and reoxidation of poly(DPP-TPD) in aqueous (aq.) 0.1 M KCl are depicted. The difference in absorption (ΔOD) obtained by subtracting the absorption at definite wavelengths of pristine film from reduced/oxidized samples is included in **Figure S5** in the Supporting Information. The absolute values of optical density of the pristine film (in **Figure 3a**) and the reoxidized film (in **Figure 3b**) at 740 nm are not identical, indicating that the reduced species may undergo some changes leading to spectral changes during the redox process. The polaron absorption, in contrast, vanishes completely. This behavior is further visualized in **Figure 3c**, where the ΔOD at 740 nm (pristine absorption) and 1050 nm (polaron absorption) are depicted together. While the polaron absorption shows little hysteresis, a pronounced offset is apparent in the plateau values of the ground state absorption maximum at 740 nm. Considering the long measurement time of more than 1 h for one set of SEC data in an aqueous medium under ambient conditions, this can be expected if the reduced species undergo further reactions under these conditions.

To evaluate the suitability of poly(DPP-TPD) as an n-type semiconductor in general, organic field effect transistor (OFET) devices were fabricated. Doped Si bottom gate, gold bottom contact devices with thermally grown SiO_x layer, modified with an hexamethyldisilazane (HMDS) monolayer were

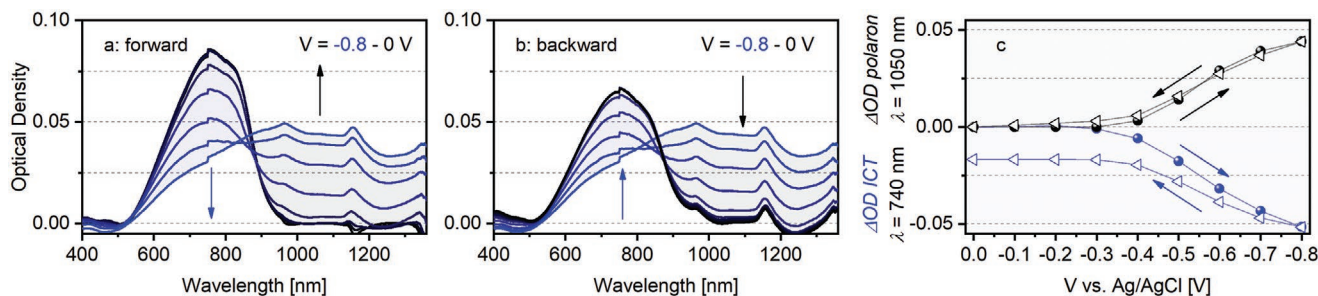


Figure 3. SEC spectra for a) forward and b) backward electrochemical reduction of poly(DPP-TPD) on ITO substrates, in aq. 0.1 M KCl. Potentials are relative to a Ag/AgCl reference electrode. c) Difference of the peak maxima of the ground state and polaron absorption, relative to the applied potential during forward and backward scans.

used for this investigation. Both transfer and output characteristics (Figure S6, Supporting Information) indicate unipolar electron transport without any hole conduction with $\mu_e = 4.4 \times 10^{-4} \text{ cm}^2 \text{ V}^{-1} \text{ s}^{-1}$ and $V_{\text{th}} = 35.3 \text{ V}$ when measured under an inert atmosphere. Under ambient conditions, transistor switching takes place on a longer timescale, as shown in Figure S7 in the Supporting Information. Unipolar electron conduction as well as solvent processability opens up further applications, like as electron transport layer (ETL) in organic or perovskite solar cells. As fitting orthogonal solvents exist (dimethylformamide (DMF) for perovskite active layers, toluene for organic active layers), poly(DPP-TPD) can be incorporated in both conventional and inverted stacks. Another possibility is to use such polymers in their n-doped state in thermoelectric devices.^[35]

2.4. OECT Characterization

Poly(DPP-TPD) fulfills the fundamental conditions necessary for OECT application: OFET and CV studies reveal that unidirectional n-type transport is favored. Further, SEC demonstrated reduction at a relatively low onset voltage of $\approx 300 \text{ mV}$ in aqueous medium. Together, these results suggest the high suitability of poly(DPP-TPD) as n-type material for bioelectronic applications. Hence, the real applicability of poly(DPP-TPD) was put to the test by the fabrication of OECTs with the polymer as active channel material. The architecture of the used devices is depicted schematically in Figure 4a and consisted of interdigitated gold source and drain electrodes, gated with a Ag/AgCl electrode in an aqueous 0.1 M KCl solution.

Drain sweeps in Figure 4b show well-defined n-type output behavior with a pinch-off point at $\approx 200 \text{ mV}$ at $V_g = 0.8 \text{ V}$ and a steady current of $I_{\text{max}} = 80 \mu\text{A}$ at drain voltages above 200 mV. For quantification of the aforementioned benchmark values μC^* and V_{th} , transfer characteristics were recorded. Linear extrapolation of the square root of the drain current to $I_d^{0.5} = 0 \text{ A}^{0.5}$, the X-axis intercept, reveals a threshold voltage of $V_{\text{th}} = 570 \text{ mV}$, as depicted in Figure S8a in the Supporting Information. By forming the first derivative, dI/dV , the transconductance was calculated, as plotted in Figure 4c. The maximum transconductance of $g_m = 822 \mu\text{S}$ presents an extraordinarily high value for n-type materials. For comparative purposes, this value was also normalized by film thickness and the electrode dimensions to obtain a transconductance $g_m' = 1.31 \text{ S cm}^{-1}$. The sub-threshold

swing was calculated to be $dV = 68 \text{ mV dec}^{-1}$ (cf. Figure S8b, Supporting Information). To determine μC^* of poly(DPP-TPD), transfer curves were processed by plotting transconductance against device geometry factor, Wd/L (W and L being width and length of the channel and d being the thickness of the semiconductor layer) yielding the plots in Figure 4d where the slope of the linear regime corresponds to μC^* of the material. As indicated in Figure 4, an average μC^* of $(7.62 \pm 0.32) \text{ F cm}^{-1} \text{ V}^{-1} \text{ s}^{-1}$ and champion value of $8.05 \text{ F cm}^{-1} \text{ V}^{-1} \text{ s}^{-1}$ was reached. Further, the potential-dependent volumetric capacitance was measured by electrochemical impedance spectroscopy (Figure S9, Supporting Information). Taking electrochemical impedance spectroscopy (EIS) measurements for C^* determination into account, both parameters μ_{OECT} and C^* can be deconvoluted, and the electron mobility in the swollen state, μ_{OECT} , determined, as listed in Table 1. Due to the direct inaccessibility of μ_{OECT} , however, this value must only be considered as an approximation. Overall, the low errors of the values, averaged over six devices also demonstrate the excellent reproducibility of the OECT characteristics, as indicated in Figure S10 and Table S2 in the Supporting Information. The details of all OECT devices are given in Table S2 in the Supporting Information.

To put the rest of our findings in perspective, for an n-type OECT, the determined threshold voltage of $V_{\text{th}} = 0.58 \text{ V}$ is relatively low, while the average μC^* is outstandingly high. Most state-of-the-art n-type systems are either based on Poly(benzimidazobenzophenanthroline) or poly(naphthalene diimide) (PNDI)-derived D-A copolymers. Despite the high μC^* values of the former material of up to $\mu C^* = 26 \text{ F cm}^{-1} \text{ V}^{-1} \text{ s}^{-1}$, the low processability of the material makes it nonoptimal for applications.^[15] PNDI-based systems, on the other hand, are readily soluble in common organic solvents, and thus became the working horse in the field of n-type OECT research. By variations of the polymer structure, μC^* values of $1.29 \text{ F cm}^{-1} \text{ V}^{-1} \text{ s}^{-1}$ were reached.^[36]

2.5. OECT Cycling Stability and Response Time

For long-term usage, the operation stability of the active layer material is a vital prerequisite. Prolonged device operation was simulated by repeatedly switching on and off a freshly prepared OECT device with poly(DPP-TPD) as active n-channel material while monitoring the drain current. Devices were cycled in the saturation regime at a drain voltage of $V_d = 0.4 \text{ V}$ (cf. Figure 4).

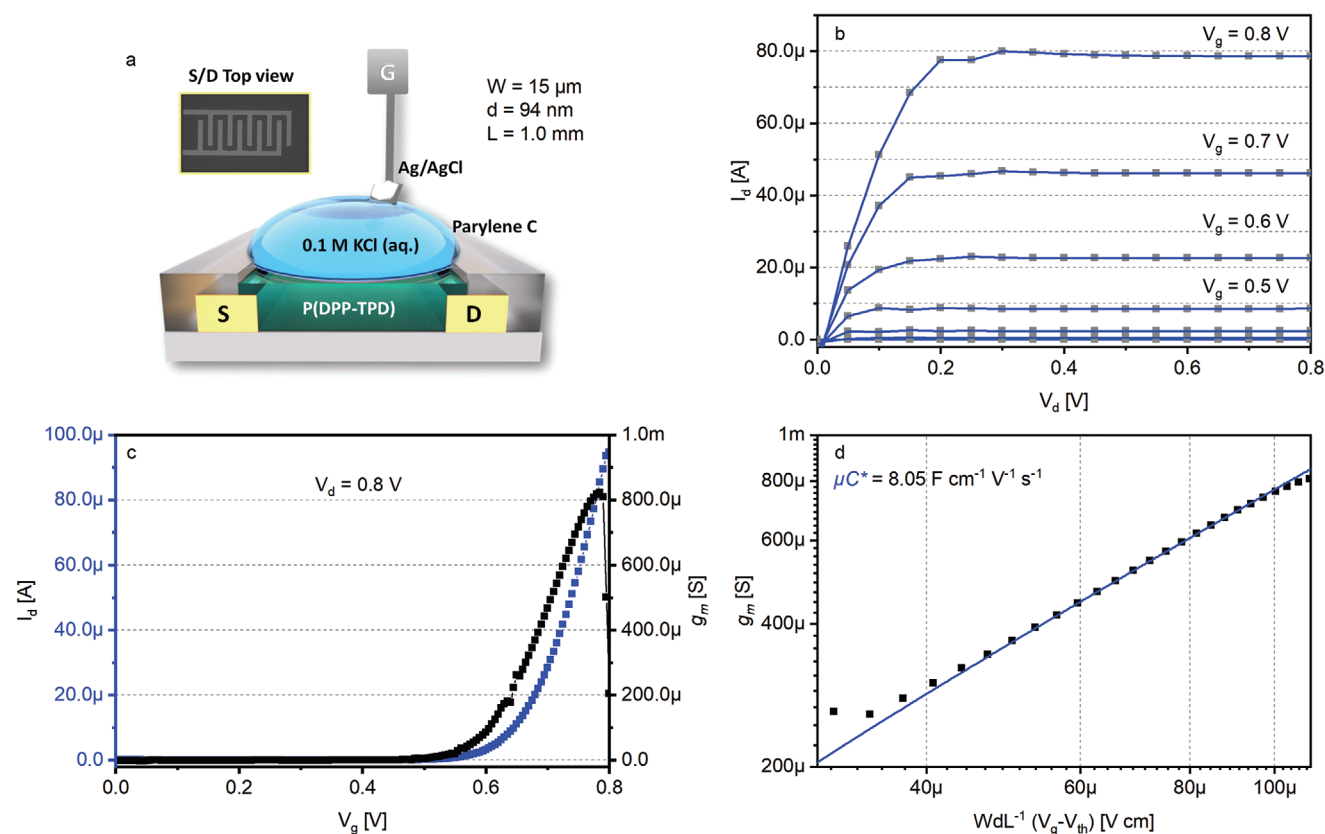


Figure 4. n-Type OEET curves, measured on the devices schematically shown in (a), consisting of interdigitated gold electrodes, gated by an Ag/AgCl electrode in 0.1 m KCl. b) Output characteristics at V_g between 0 and 0.8 V. c) Transfer characteristics and transconductance at $V_d = 0.8$ V. d) Device geometry-adjusted V_g versus transconductance used for μC^* determination. The depicted curves belong to the device with the highest μC^* value.

The gate potential on the same device was increased stepwise from $V_g = 0.6$ V to $V_g = 0.7$ V and finally, $V_g = 0.8$ V. Each cycle consisted of one second without applied drain bias (“off-state”), followed by one second under applied bias (“on-state”). Consequently, 30 min of device sampling corresponds to 900 on-off cycles. After this first 30 min cycling, the gate voltage was increased and the measurement cycles were repeated resulting in a total cycling time of 90 min. Thus, all sampling studies were conducted consecutively on the same device, adding up

to a total stress of 2700 on-off cycles (in 90 min). As depicted in **Figure 5**, a slight decrease in drain current is observable under all sampling conditions. However, as expected, the current retention depends on the gate voltage applied. The higher the gate voltage applied, the lower the current retention, hinting at either side reactions of the reduced species in water and ambient conditions, which agrees qualitatively with the limited reversibility of the reduction process, observed in SEC studies, or kinetic effects limiting the current. While high

Table 1. Overview of the basic and OEET-related polymer properties of poly(DPP-TPD). OEET values were averaged over a minimum of six datasets from 0.1 m KCl (aq.) gated devices in the saturation regime ($V_d = 0.8$ V). $W = 15$ μm , $d = 94$ nm, and $L = 1$ mm.

M_n^a [kg mol ⁻¹]	\mathcal{D}^a	$T_{5\%}^b$ [°C]	μ_e^c [cm ² V ⁻¹ s ⁻¹]	V_{th}^d [V]	EA_{aq}^d [eV]	EA_{MeCN}^e [eV]	IP^f [eV]
20.6	1.8	306	4.4×10^{-4}	35.3	4.01	4.15	5.2
Polaron abs. onset ^g [V]	V_{th}^h [mV]	$g_m(max)^i$ [μS]	$g_m'(max)^j$ [S cm ⁻¹]	C_{max}^k [F cm ⁻³]	μC^*^l [F cm ⁻¹ V ⁻¹ s ⁻¹]	μ_{OEET}^m [cm ² V ⁻¹ s ⁻¹]	S_{24}^n [mV]
0.3	575 ± 9	821 ± 32	1.31 ± 0.05	68.58	7.62 ± 0.32	0.11	68.2 ± 1.3

^a) Number average molecular mass and dispersity were determined via GPC using HFIP versus PMMA calibration; ^b) Determined by TGA under N₂ atmosphere at a heating rate of 10 K min⁻¹; ^c) OFET mobility and threshold were determined in the saturation regime of annealed films (15 min at 150 °C) on BC (Si/SiO₂/HMDS) BC (Au) devices; ^d) Determined via CV in thin films on ITO coated glass in 0.1 m aq. KCl; ^e) Determined via DPV in thin films on ITO-coated glass in 0.1 m TBABF in MeCN solutions; ^f) Determined from the SECO and VBM onset in UPS; ^g) Determined from the onset of polaron absorption in SEC measurements; ^h) Extracted from the linear fit of the plot $I_d^{0.5}$ versus V_g in the OEET saturation regime; ⁱ) Average maximum OEET transconductance; ^j) device architecture-independent transconductance, obtained by normalization of g_m with $W^{-1}d^{-1}L$; ^k) Extracted from EIS measurements in 0.1 m aq. KCl electrolyte at $V = -0.6$ V; ^l) Extracted from the slope of $WdL^{-1}(V_g - V_{th})$ versus g_m in the saturation regime; ^m) Calculated from μC^* and C^* ; ⁿ) Extracted from the linear fit of the plot $\log(I_d)$ versus V_g in the OEET saturation regime.

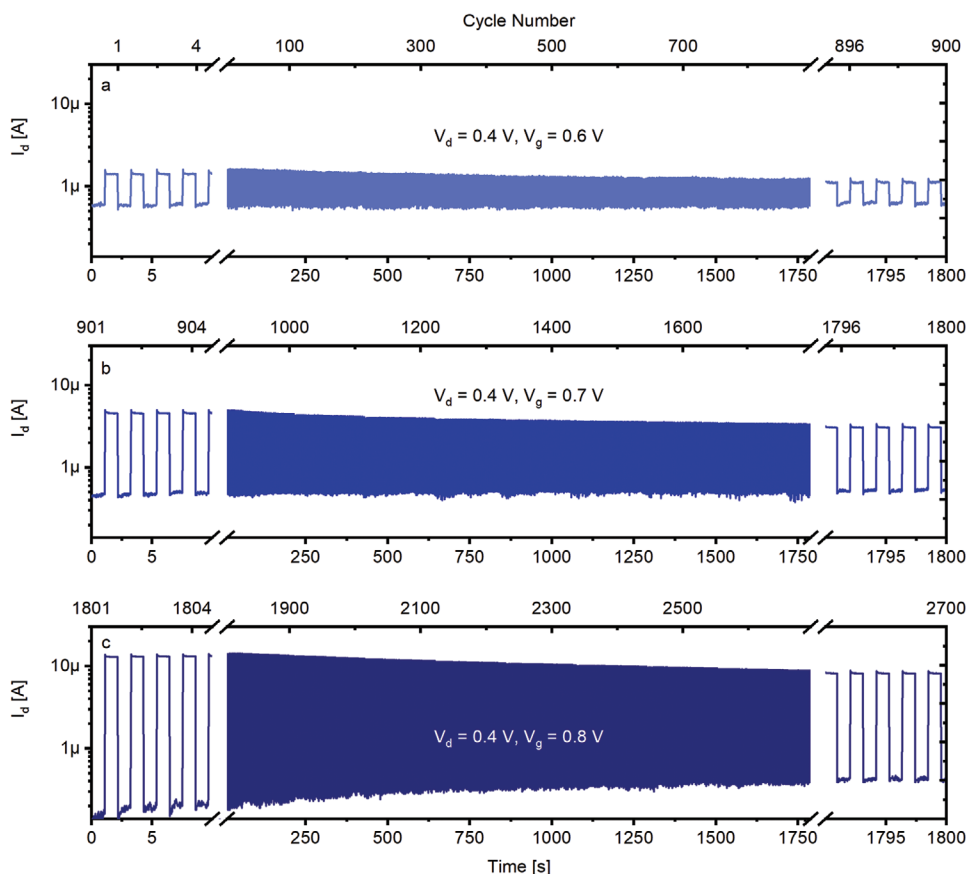


Figure 5. Long-time cycling of the polymer poly(DPP-TPD) at increasing gate voltages ranging from a) 0.6 V to b) 0.7 V and c) 0.8 V using aq. 0.1 M KCl as the electrolyte. The drain voltage for cycling was 0.4 V. A cycle consisted of 1 s of applied gate and drain potential, followed by 1 s with zero drain voltage. The same sample was subjected to 3×900 cycles with increasing potentials.

current retention of 82.0% is reached at a gate voltage of 0.6 V, it decreases to 70.9% at $V_g = 0.7$ and 65.0% at $V_g = 0.8$ V after 2700 cycles. The exact values of current retention are listed in **Table 2**. The respective off-current values (I_{off}) for gate potential, V_g of 0.6, 0.7, and 0.8 V are 600, 480, and 150 nA, respectively. Thus on changing the gate potential from 0.6 to 0.7 and 0.8 V, a decreasing trend in I_{off} can be observed. (cf. Figure 5a–c). This behavior can be explained if the gate leakage current during cycling, as depicted in Figure S11 in the Supporting Information, is considered. During the off-state of the transistor, the gate leakage current is relatively high, as injected charges are not efficiently harvested via the drain electrode. Instead it leads to potential-driven current flow to the gate electrode. Upon increase of the gate potential, despite a higher

Table 2. Current retention after switching an OECT on and off for 900 consecutive times at each gate potential. Each on- and off period lasted 1 s, resulting in 30 min of stress per step. All measurements were performed successively on the identical device.

V_d [mV]	V_g [mV]	Current retention after 30 min or 900 cycles [%]
400	600	82.0
400	700	70.9
400	800	65.0

degree of chemical reduction (doping) of the active material, the drain off-current slightly decreases, because the increased gate potential leads to a higher extent of charge carrier leakage toward the gate electrode, instead of the drain electrode.

Under extreme stress conditions of the high number of on–off cycles, the observed current retention values are outstanding in the context of n-type OECT materials. This showcases the viability of acceptor–acceptor materials with low-lying LUMO for OECT applications.

Next, we investigated the response time of a single on- and off-switching event with increased time resolution. To determine the switching speed of poly(DPP-TPD), rectangular potentials were applied simultaneously via the gate and drain electrodes as depicted in Figure S12 in the Supporting Information for $V_g = V_d = 0.7$ V and Figure S13 in the Supporting Information for $V_g = V_d = 0.8$ V. Neither on- nor off-switching did represent ideal exponential behavior, hinting the interplay of different electrochemical processes such as ion diffusion and polymer reduction. Therefore, the velocity of on- and off-switching were determined at times where 90% of the maximum current was reached during on-switching ($\tau_{90\text{-on}}$) and 90% decrease of the maximum current for off-switching ($\tau_{90\text{-off}}$). For a gate and drain potential of 0.7 V, switching times of $\tau_{90\text{-on}} = 17.2$ and $\tau_{90\text{-off}} = 4.0$ ms were observed, which decreased to $\tau_{90\text{-on}} = 12.5$ ms and $\tau_{90\text{-off}} = 0.6$ ms when the increased gate and drain potentials of 0.8 V were

applied. Rapid switching kinetics as demonstrated for this material here is, e.g., required for circuitry applications or precise time-resolved bioelectronic monitoring.

3. Conclusion

By the rational combination of the two electron-deficient building blocks DPP and TPD, a new hydrophilic acceptor–acceptor copolymer poly(DPP-TPD) was designed and synthesized using direct arylation polymerization in a microwave reactor. The design was focused on lowering the LUMO level as well as the planarization of the polymer chain by reducing the torsional angles. Monomer synthesis was streamlined starting from literature-known procedures and polymerized subsequently via direct arylation polymerization. By employing microwave-assisted synthesis, low reaction times and temperatures were achieved. The purified polymer was first evaluated concerning its suitability for OECT application based on its optoelectronic properties. Cyclic voltammetry in H₂O/KCl and differential pulse voltammetry in MeCN/Bu₄N⁺BF₄⁻ showed low LUMO values below 4 eV, suitable for stable operation under ambient conditions. UV–vis spectroelectrochemistry further demonstrated reduction in aqueous media, complemented by moderate OFET electron mobilities of $4.4 \times 10^{-4} \text{ cm}^2 \text{ V}^{-1} \text{ s}^{-1}$.

N-type accumulation mode OECT characterization revealed an outstanding average μC^* of $(7.62 \pm 0.32) \text{ F cm}^{-1} \text{ V}^{-1} \text{ s}^{-1}$, moderate threshold voltage (575 ± 9) mV, and low sub-threshold swing of $(68.2 \pm 1.3) \text{ mV dec}^{-1}$. Further, rapid response kinetics with switching speeds of up to $\tau_{90\text{-on}} = 12.5$ and $\tau_{90\text{-off}} = 0.6$ ms were demonstrated. Dynamic stress studies demonstrate outstanding cycling stability after a total of 2700 cycles and a current retention of 65.0% after 900 cycles at a gate voltage of 800 mV in the saturation regime in aqueous medium under ambient conditions. The high benchmark values, in combination with the streamlined, relatively nontoxic synthesis makes this system optimal for further studies to optimize the stability and performance of n-type mixed conductors.

4. Experimental Section

Synthesis: $P(\text{DPP}[\text{T}]_2\{\text{TEG}\}\text{-TPD}\{\text{TEG}\})/\text{poly}(\text{DPP-TPD})$: The monomers TPD{TEG} (0.04 g, 0.15 mmol, 1 eq.) and DPP[T]₂{TEG}-Br₂ (0.113 g, 0.15 mmol, 1 eq.), ligands pivalic acid (4.6 mg, 0.045 mmol, 0.3 eq.) and tris(2-methoxyphenyl)phosphine (4.2 mg, 0.012 mmol, 0.08 eq.), the base Cs₂CO₃ (0.114 g, 0.35 mmol, 2.32 eq.) and catalyst Pd-Hermann (2.8 mg, 3.0 μmol, 0.02 eq.) were weighed in this order in a microwave vial under ambient conditions. A stir bar was added and the vial was sealed with a septum. The septum is punctured with a canula and placed in a Schlenk flask. After the application of high vacuum on the solids for 15 min, the vessels were backfilled with argon, followed by the removal of the canula with the microwave vial still in the Schlenk flask. 0.6 mL (0.25 M, relative to monomer TPD{TEG}) anhydrous *o*-xylene is added to the vial and purged for 20 min under rapid stirring. Polymerization is conducted for 2 h at 160 °C under microwave irradiation. Afterward, the polymerization mixture is diluted with chloroform, precipitated in methanol, and filtered through a cellulose Soxhlet thimble. Oligomer, catalyst, and additive residues are removed by extraction with methanol, followed by 2-butanone. The remaining polymer is redissolved in hexafluoro isopropanol and precipitated in

water, to ensure quantitative carbonate removal. 0.082 g (62%) polymer is obtained as a black powder.

¹H NMR (300 MHz, CDCl₃, δ): 7.56 (s, 2 H), 6.5 (s, 2 H), 2.70–4.60 (broad, 56 H), (cf. Figure S1, Supporting Information).

2,5-Bis(2-(2-(2-methoxyethoxy)ethoxy)ethyl)-3,6-di(5-bromothiophen-2-yl)pyrrolo[3,4-c]pyrrole-1,4(2H,5H)-dione/DPP[T]₂{TEG}-Br₂: A dried Schlenk flask was charged with DPP[T]₂{TEG} and kept under high vacuum (HV) for 15 min. After backfilling with argon, anhydrous CHCl₃ was added. The solution was cooled to 0 °C under stirring, the flask was wrapped in aluminum foil and N-bromosuccinimide was added under Ar counter flow. The ice bath was removed and the reaction was allowed to progress at room temperature (RT) for 4 d. After workup with aq. HNaCO₃ (sat.), the solution was concentrated and poured into a large excess of methanol. The solution was stored overnight at –25 °C to encourage crystallization. The crystalline product was filtered and washed with cold methanol. After column chromatography (silica, gradient dichloromethane (DCM) → ethyl acetate, product in second fraction), and subsequent solvent removal, 2.7 g (3.6 mmol, 53%) pure product is obtained as a metallic red powder.

¹H NMR (300 MHz, CDCl₃, δ): 8.49 (d, *J* = 4.14 Hz, 2 H), 7.21 (d, *J* = 4.33 Hz, 2 H), 4.17 (t, *J* = 5.93 Hz, 4 H), 3.78 (t, 4 H), 3.46–3.67 (m, 16 H), 3.35 (s, 6 H).

2,5-bis(2-(2-(2-methoxyethoxy)ethoxy)ethyl)-3,6-di(thiophen-2-yl)pyrrolo[3,4-c]pyrrole-1,4(2H,5H)-dione/DPP[T]₂{TEG}: A dried Schlenk flask was charged with DPP[T]₂ (4.0 g, 13.3 mmol, 1 eq.), freshly dried (HV, 500 °C) K₂CO₃ (7.37 g, 53.3 mmol, 4 eq.) and 18-crown-6 (0.176 g, 0.67 mmol, 0.05 eq.) and kept under HV for 15 min. After carefully backfilling the flask with argon, anhydrous DMF (82.5 mL, 0.16 M, relative to DPP[T]₂) was added. The dispersion was heated to 110 °C for 1 h and subsequently cooled to 0 °C, where TEG-Br (9.99 g, 44.0 mmol, 3.3 eq.) was added slowly. The reaction mixture was allowed to heat to room temperature and heated to 130 °C for 24 h. After the reaction mixture reached RT, it was washed with brine three times. The combined aqueous phases were extracted with chloroform. The combined organic phases were dried over MgSO₄, followed by filtration and complete solvent removal in vacuo. The dry crude product was redissolved in a small amount of chloroform, poured into a large excess of MeOH, and stored at –25 °C overnight. 2.0 g (3.4 mmol, 25%) pure product is obtained as red crystals.

¹H NMR (300 MHz, CDCl₃, δ): 8.75 (dd, *J* = 3.96, 1.13 Hz, 2 H), 7.63 (dd, *J* = 4.90, 1.13 Hz, 2 H), 7.23–7.28 (m, 2 H), 4.27 (t, *J* = 6.31 Hz, 4 H), 3.78 (t, 4 H), 3.45–3.67 (m, 16 H), 3.34 (s, 6 H).

3,6-Di(thiophen-2-yl)-2,5-bis(2-hexyldodecyl)-pyrrolo[3,4-c]pyrrole-1,4-dione/DPP[T]₂: In a three-necked 500 mL round-bottom flask sodium-2-methylbutan-2-oleate (19 g/172 mmol) was dissolved in dry 2-methylbutan-2-ol (70 mL) at 100 °C. Thiophene-2-carbonitrile (12.5 g/115 mmol) was added in one part and diethyl succinate (10 g/57 mmol) was added slowly (3 mL h⁻¹) using a syringe-pump and the resulting dark red mixture was stirred overnight at 100 °C. Thereafter, it was cooled to 65 °C, and methanol (200 mL) was added carefully. Acetic acid (11 mL) was added to neutralize the mixture and precipitate the crude product which was filtered off, while still warm. The crude solid was washed with methanol and water, dried at 40 °C in vacuo, and used as obtained. Yield: 8.8 g (29 mmol/51%) of a dark red solid.

¹H NMR (300 MHz, dimethyl sulfoxide (DMSO)-d₆, δ): 10.39 (br. s., 2 H), 7.35 (dd, *J* = 3.86, 1.22 Hz, 2 H), 7.10 (dd, *J* = 4.90, 1.13 Hz, 2 H), 6.44 (dd, *J* = 4.90, 3.77 Hz, 2 H).

1-(Bromomethoxy)-2-(2-methoxyethoxy)ethane/TEG-Br: 2-(2-(2-methoxyethoxy)ethoxy)ethan-1-ol (TEG-OH, 20 g, 122 mmol, 1 eq.) and CBr₄ (52.5 g, 158 mmol, 1.3 eq.) were dissolved in DCM (200 mL, 0.61 M, relative to TEG-OH) and cooled to 0 °C. PPh₃ (44.7 g, 171 mmol, 1.4 eq.) is dissolved in DCM (50 mL, 3.41 M, relative to PPh₃) and added dropwise via an addition funnel. The reaction mixture was stirred for 45 min at this temperature, then it was allowed to heat to RT and react at this temperature for another 45 min. The reaction mixture was poured into a 1: 4 (v: v) mixture of diethyl ether and hexanes, followed by filtration over a silica plug. Upon solvent removal in vacuo, the mixture partially solidified. The crude mixture was distilled in vacuo,

first without active cooling to avoid bromoform solidification. 27.2 g (120 mmol, 98%) pure product was obtained as a colorless liquid.

¹H NMR (300 MHz, CDCl₃, δ): 3.80 (t, *J* = 6.4 Hz, 2 H), 3.71–3.62 (m, 6H), 3.58–3.52 (m, 2 H), 3.46 (t, *J* = 6.3 Hz, 2 H), 3.37 (s, 3 H).

5-((2-(2-Methoxyethoxy)ethoxy)methyl)-4H-thieno[3,4-*c*]pyrrole-4,6(5H)-dione/TPD{TEG}: A Schlenk flask was charged with TPD (2 g, 13 mmol, 1 eq.) and freshly dried (HV, 500 °C) K₂CO₃ (3.60 g, 26.1 mmol, 2 eq.). Anhydrous DMF (52 mL) was added, followed by the addition of previously HV-degassed TEG-Tos (4.07 g, 12.8 mmol, 0.98 eq.). The reaction was stirred at 110 °C overnight. After cooling to room temperature, the product solution was stirred with water and extracted three times with DCM. The combined organic phases were dried with MgSO₄. During solvent removal in vacuo, a solid formed that was purified by recrystallization from boiling methanol to yield 2.6 g (56.7 mmol, 87%) white solid product.

¹H NMR (300 MHz, CDCl₃, δ): 7.80 (s, 2 H), 3.70–3.78 (m, 2 H), 3.60–3.67 (m, 2 H), 3.63–3.41 (m, 8 H), 3.30 (s, 3 H).

Thieno[3,4-*c*]pyrrole-4,6(5 H)-dione/TPD: 3,4-Thiophenedicarboxylic acid (13 g, 75.5 mmol, 1 eq.), water (7.55 mL), and ammonia (25% in water, 51.4 g, 755 mmol, 10 eq.) were added to a round bottom flask, equipped with glass beads. The reaction mixture was heated to 95 °C and allowed to remain at this temperature to react, accompanied by the removal of the solvent. When no solvent remained, a condenser was attached to the flask and the temperature increased to 260 °C. The product partly resublimed on the condenser but was mostly contained in the flask, together with dark impurities. After 4 h at 260 °C, the reaction was cooled to RT, and all solids were collected together and resublimed on a coldfinger, to yield 9.3 g (60.7 mmol, 80%) white solid.

¹H NMR (300 MHz, DMSO-*d*₆, δ): 11.25 (b, 1 H), 8.25 (s, 2 H).

(2-(2-Methoxyethoxy)ethoxy)methyl 4-methylbenzenesulfonate/TEG-Tos: 2-(2-(2-methoxyethoxy)ethoxy)ethan-1-ol (26.3 g, 160 mmol, 1 eq.) and tosyl chloride (32.1 g, 168 mmol, 1.05 eq.) were dissolved in DCM (114 mL, 1.4 M relative to TEG-OH) and cooled to 0 °C. KOH (35.9 g, 641 mmol, 4 eq.) was added portionwise and slowly. The ice bath was allowed to thaw and the reaction was stirred for 3 d. After workup with diluted HCl, the solution was dried with MgSO₄ and the solvent was removed. 50 g (157 mmol, 98%) pure compound was obtained without further purification as colorless liquid.

¹H NMR (300 MHz, CDCl₃, δ): 7.85–7.74 (m, 2 H), 7.34 (dd, *J* = 8.6, 0.6 Hz, 2 H), 4.19–4.11 (m, 2 H), 3.72–3.64 (m, 2 H), 3.63–3.56 (m, 6 H), 3.55–3.48 (m, 2 H), 3.36 (s, 3 H), 2.44 (s, 3 H).

Instruments and Methods: A detailed description of experimental methods (UPS, OFET fabrication and evaluation, OECT fabrication and evaluation, GIWAXS, NMR spectroscopy, EIS, TGA, flash DSC, SEC, UV-vis, CV, and DPV) can be found in the Supporting Information.

Supporting Information

Supporting Information is available from the Wiley Online Library or from the author.

Acknowledgements

The authors acknowledge financial support from Deutsche Forschungsgemeinschaft (DFG) (TH 807/7-1) and the Bavarian State Ministry for Science and Art (SolTech). The authors acknowledge the KeyLab Surface and Interface Characterization of the Bavarian Polymer Institute (University of Bayreuth), Markus Hund, and Nicolas Helfricht for providing AFM measurements and support during the evaluation. This work was supported by a fellowship of the German Academic Exchange Service (DAAD). The authors thank Linjing Tang for support in recording pulsed potential measurements and Wen Liang Tan for assistance during GIWAXS experiments. This work was performed in part at the SAXS/WAXS beamline at the Australian Synchrotron, part of Australian Nuclear Science and Technology Organisation (ANSTO).^[37]

Open access funding enabled and organized by Projekt DEAL.

Conflict of Interest

The authors declare no conflict of interest.

Data Availability Statement

The data that support the findings of this study are available from the corresponding author upon reasonable request.

Keywords

acceptor–acceptor, bioelectronics, direct arylation polymerization, double acceptor polymers, n-type OECT

Received: January 13, 2023

Revised: March 17, 2023

Published online: May 1, 2023

- [1] M. Sommer, in *Organic Flexible Electronics: Fundamentals, Devices and Applications*, Woodhead Publishing, Duxford [England]; Cambridge, MA 2021, pp. 27–70.
- [2] S. Darabi, C.-Y. Yang, Z. Li, J.-D. Huang, M. Hummel, H. Sixta, S. Fabiano, C. Müller, *Adv. Electron. Mater.*, <https://doi.org/10.1002/aelm.202201235>.
- [3] X. Xu, Y. Zhao, Y. Liu, *Small*, <https://doi.org/10.1002/smll.202206309>.
- [4] K. Ditte, T. A. Nguyen Le, O. Ditzer, D. I. Sandoval Bojorquez, S. Chae, M. Bachmann, L. Baraban, F. Lissel, *ACS Biomater. Sci. Eng.* 2021, acsbiomaterials.1c00727, <https://doi.org/10.1021/acsbomaterials.1c00727>.
- [5] D. Khodagholy, T. Doublet, P. Quilichini, M. Gurfinkel, P. Leleux, A. Ghestem, E. Ismailova, T. Hervé, S. Sanaur, C. Bernard, G. G. Malliaras, *Nat. Commun.* 2013, 4, 1575.
- [6] D. A. Bernards, G. G. Malliaras, *Adv. Funct. Mater.* 2007, 17, 3538.
- [7] E. Zeglio, O. Inganäs, *Adv. Mater.* 2018, 30, 1800941.
- [8] S. Inal, J. Rivnay, P. Leleux, M. Ferro, M. Ramuz, J. C. Brendel, M. M. Schmidt, M. Thelakkat, G. G. Malliaras, *Adv. Mater.* 2014, 26, 7450.
- [9] S.-M. Kim, C.-H. Kim, Y. Kim, N. Kim, W.-J. Lee, E.-H. Lee, D. Kim, S. Park, K. Lee, J. Rivnay, M.-H. Yoon, *Nat. Commun.* 2018, 9, 3858.
- [10] J. C. Brendel, M. M. Schmidt, G. Hagen, R. Moos, M. Thelakkat, *Chem. Mater.* 2014, 26, 1992.
- [11] S. Inal, G. G. Malliaras, J. Rivnay, *Nat. Commun.* 2017, 8, 1767.
- [12] Y. Wang, E. Zeglio, H. Liao, J. Xu, F. Liu, Z. Li, I. P. Maria, D. Mawad, A. Herland, I. McCulloch, W. Yue, *Chem. Mater.* 2019, 31, 9797.
- [13] A. Weissbach, L. M. Bongartz, M. Cucchi, H. Tseng, K. Leo, H. Kleemann, *J. Mater. Chem. C* 2022, 10, 2656.
- [14] P. Schmode, A. Savva, R. Kahl, D. Ohayon, F. Meichsner, O. Dolynchuk, T. Thurn-Albrecht, S. Inal, M. Thelakkat, *ACS Appl. Mater. Interfaces* 2020, 12, 13029.
- [15] H.-Y. Wu, C.-Y. Yang, Q. Li, N. B. Kolhe, X. Strakosas, M.-A. Stoeckel, Z. Wu, W. Jin, M. Savvakis, R. Kroon, D. Tu, H. Y. Woo, M. Berggren, S. A. Jenekhe, S. Fabiano, *Adv. Mater.* 2022, 34, 2106235.
- [16] A. Giovannitti, C. B. Nielsen, D.-T. Sbircea, S. Inal, M. Donahue, M. R. Niazi, D. A. Hanifi, A. Amassian, G. G. Malliaras, J. Rivnay, I. McCulloch, *Nat. Commun.* 2016, 7, 13066.
- [17] Y. Zhang, G. Ye, T. P. A. Van Der Pol, J. Dong, E. R. W. Van Doremale, I. Krauhausen, Y. Liu, P. Gkoupidenis, G. Portale, J. Song, R. C. Chiechi, Y. Van De Burgt, *Adv. Funct. Mater.* 2022, 32, 2201593.
- [18] D. M. De Leeuw, M. M. J. Simenon, A. R. Brown, R. E. F. Einerhand, *Synth. Met.* 1997, 87, 53.

- [19] H. Usta, C. Risko, Z. Wang, H. Huang, M. K. Deliomeroğlu, A. Zhukhovitskiy, A. Facchetti, T. J. Marks, *J. Am. Chem. Soc.* **2009**, *131*, 5586.
- [20] X.-Q. Chen, X. Yao, T. Bai, J. Ling, W.-J. Xiao, J. Wang, S.-C. Wu, L.-N. Liu, G. Xie, J. Li, Z. Lu, I. Visoly-Fisher, E. A. Katz, W.-S. Li, *J. Polym. Sci., Part A: Polym. Chem.* **2018**, *56*, 689.
- [21] M. Goel, C. D. Heinrich, G. Krauss, M. Thelakkat, *Macromol. Rapid Commun.* **2019**, *40*, 1800915.
- [22] C. Kanimozhi, M. Naik, N. Yaacobi-Gross, E. K. Burnett, A. L. Briseno, T. D. Anthopoulos, S. Patil, *J. Phys. Chem. C* **2014**, *118*, 11536.
- [23] C. J. Mueller, C. R. Singh, M. Fried, S. Huettnner, M. Thelakkat, *Adv. Funct. Mater.* **2015**, *25*, 2725.
- [24] L. Q. Flagg, C. G. Bischak, J. W. Onorato, R. B. Rashid, C. K. Luscombe, D. S. Ginger, *J. Am. Chem. Soc.* **2019**, *141*, 4345.
- [25] T. Weller, M. Breunig, C. J. Mueller, E. Gann, C. R. McNeill, M. Thelakkat, *J. Mater. Chem. C* **2017**, *5*, 7527.
- [26] T. Weller, K. Rundel, G. Krauss, C. R. McNeill, M. Thelakkat, *J. Phys. Chem. C* **2018**, *122*, 7565.
- [27] C. J. Mueller, C. R. Singh, M. Thelakkat, *J. Polym. Sci., Part B: Polym. Phys.* **2016**, *54*, 639.
- [28] J. Warnan, C. Cabanetos, A. E. Labban, M. R. Hansen, C. Tassone, M. F. Toney, P. M. Beaujuge, *Adv. Mater.* **2014**, *26*, 4357.
- [29] S. Yum, T. K. An, X. Wang, W. Lee, M. A. Uddin, Yu J. Kim, T. L. Nguyen, S. Xu, S. Hwang, C. E. Park, H. Y. Woo, *Chem. Mater.* **2014**, *26*, 2147.
- [30] J.-R. Pouliot, L. G. Mercier, S. Caron, M. Leclerc, *Macromol. Chem. Phys.* **2013**, *214*, 453.
- [31] G. Krauss, F. Meichsner, A. Hochgesang, J. Mohanraj, S. Salehi, P. Schmode, M. Thelakkat, *Adv. Funct. Mater.* **2021**, *31*, 2010048.
- [32] R. M. W. Wolfe, J. R. Reynolds, *Org. Lett.* **2017**, *19*, 996.
- [33] Y. Shi, H. Guo, M. Qin, Y. Wang, J. Zhao, H. Sun, H. Wang, Y. Wang, X. Zhou, A. Facchetti, X. Lu, M. Zhou, X. Guo, *Chem. Mater.* **2018**, *30*, 7988.
- [34] D. Hashemi, X. Ma, R. Ansari, J. Kim, J. Kieffer, *Phys. Chem. Chem. Phys.* **2019**, *21*, 789.
- [35] A. Hochgesang, A. Erhardt, J. Mohanraj, M. Kuhn, E. M. Herzig, S. Olthof, M. Thelakkat, *Adv. Funct. Mater.*, <https://doi.org/10.1002/adfm.202300614>.
- [36] D. Ohayon, A. Savva, W. Du, B. D. Paulsen, I. Uguz, R. S. Ashraf, J. Rivnay, I. McCulloch, S. Inal, *ACS Appl. Mater. Interfaces* **2021**, *13*, 4253.
- [37] N. M. Kirby, S. T. Mudie, A. M. Hawley, D. J. Cookson, H. D. T. Mertens, N. Cowieson, V. Samardzic-Boban, *J. Appl. Crystallogr.* **2013**, *46*, 1670.